Spectrochimica Acta Part A: Molecular and Biomolecular Spectroscopy 223 (2019) 117294

Contents lists available at ScienceDirect

Spectrochimica Acta Part A: Molecular and Biomolecular Spectroscopy

journal homepage: www.elsevier.com/locate/saa

Well-tuned white-light-emitting behaviours in multicenter-Ln polyoxometalate derivatives: A photoluminescence property and energy transfer pathway study

Hechen Wu, Minna Zhi, Hanhan Chen, Vikram Singh, Pengtao Ma *, Jingping Wang, Jingyang Niu *

Henan Key Laboratory of Polyoxometalate Chemistry, College of Chemistry and Chemical Engineering, Henan University, Kaifeng, Henan 475004, China

ARTICLE INFO

Article history:
Received 11 June 2019
Accepted 18 June 2019
Available online 19 June 2019

Keywords:
Polyoxometalates
Luminescent
White light-emitting
Energy transfer

ABSTRACT

White light-emitting diodes (WLEDs) are of scientific significance in terms of their wide applications, and few uminescent materials based on white-light-emitting polyoxometalate (POM) derivatives have been reported till now. Herein, a series of organic chromophores modified POM derivatives $[N(CH_3)_4]_3K_2Ln(C_7H_5O_2)(H_2O)_2(\alpha\text{-}PW_{11}O_{39})]\cdot 11H_2O$ (Ln^{3+} = Eu^{3+} (**1**), Tb^{3+} (**2**), Tm^{3+} (**3**), Lu^{3+} (**4**)) and multicenter-Ln analogues $[N(CH_3)_4]_3K_2Eu_xTb_yTm_{1-x-y}(C_7H_5O_2)(H_2O)_2(\alpha\text{-}PW_{11}O_{39})\cdot 11H_2O$ (**5–11**) were synthesized successfully and were characterized by various physico-chemical analysis. The investigations indicate the white-light-emitting behavior can be well tuned by adjusting the molar ratio of $Eu^{3+}/Tb^{3+}/Tm^{3+}$ = 0.06:0.10:0.84 in **9**. The energy transfer process from organic benzoic and POM ligands to Eu^{3+}, Tb^{3+} and Tm^{3+} emitting centers were detected through time-resolved emission spectroscopy (TRES) and the comparison of excitation of single-, double-, treble-Ln^{3+} mixed, indicating the energy can transfer from the photoexcitation O → M LMCT state of POM components and $\pi \rightarrow \pi^*$ transition of organic ligand to sensitize the emissions of Ln^{3+} ions via intramolecular energy transition mechanism. The energy transfer between Eu^{3+} and Tb^{3+}, Tm^{3+} and Eu^{3+}, Tm^{3+} and Tb^{3+} ions also have been recorded and carefully studied by TRES and variations of Tm^{3+} luminescence lifetime in this context, and the results show a low-effectively process of energy transfer between Tm^{3+}/Eu^{3+}, Tm^{3+}/Tb^{3+} ions and a relatively good energy transfer efficiency between Eu^{3+}/Tb^{3+} ions.

1. Introduction

White light-emitting diodes (WLEDs) have been widely applied in scientific areas and technical industries because of their low cost, higher brightness, easy fabrication and low power consumption [1–4]. Lanthanide-based (Ln) materials play a pivotal role for the major applications in WLEDs, sensing, displays and so on, particularly due to their exceptional optical features such as long lifetime, high color purity and intense luminescence [5–7]. At present, the multicenter Ln^{3+}-based luminescent materials containing two or more types of Ln^{3+} ions has been found efficient enough in replacing the traditional energy-costly incandescent light bulbs [8,9]. The luminescence of Ln^{3+} ions mainly originates from the electric-dipole f-f transitions within unfilled 4f electron orbits, whereas the electric-dipole f-f transition of Ln^{3+} ions is naturally forbidden, exhibiting an extremely low molar absorption coefficient as a consequence of the same parity of 4f electron configurations (Judd-Ofelt theory) [10,11]. On account of the drawbacks, the requirements of photosensitization of ligands or matrix for generating efficient luminescence is of immense importance for the insufficiently luminescent Ln^{3+} ions [12,13].

Polyoxometalates (POMs), as the classical inorganic ligands and matrix, can be regarded as a series of metal-oxo polyhedral building blocks MO_x (M = Mo, W, V, Nb, Ta) linked by edge-, corner- or face-shared methods, which have made a notable contribution to the general knowledge of chemistry on account of their various topological structure, unexpected reactivities and potential operations such as catalytic, magnetic, optics and science materials [14–18]. In the large family of POMs, lacunary POM precursor, an inorganic multidentate ligand, can offer oxygen-rich coordination sites for binding to one or more oxophilic Ln^{3+} ions, constructing mono-, di-, tri-, tetra-, and even up to 24 nuclearity Ln-POM derivatives [19]. Furthermore, the previous works of energy-transfer process within Ln-POMs have been confirmed that POMs can be to some extent seemed as antenna materials to induce emissions of Ln^{3+} ions through intramolecular energy transfer from photoexcitation O → M ligands to metal charge transfer (LMCT) triplet states of POMs to energy-similar f-f transitions of Ln^{3+} ions [20–22]. Based on the backgrounds, plenty of Ln-POM derivatives have been reported and their optical properties were investigated.

* Corresponding authors.
E-mail addresses: mpt@henu.edu.cn (P. Ma), jyniu@henu.edu.cn (J. Niu).

https://doi.org/10.1016/j.saa.2019.117294
1386-1425/

However, the low luminous efficiency of Ln^{3+} emission sensitized by O → M LMCT photoexcitation of POMs, on account of non-radiation losses and cross-relaxation process, effectively limit their practical applications, and the reported quantum yield of most luminescent Ln-POM $[Eu(W_5O_{18})_2]^{9-}$ was about 1% [23,24]. Thus, the high-efficiency organic chromophores ligands need to be introduced into Ln-POM complexes to construct organic-inorganic hybrid chromophore-Ln-POM derivatives for improving luminescent efficiency. Till now, plenty of organic chromophores covalently modified POM derivatives have been documented, yet the ternary systems of chromophores and POM ligands directly coordinating to Ln^{3+} ions are still relatively less. In addition, almost all of above-mentioned ternary systems are pyridine-based Ln-POM derivatives, and only a few with luminescence properties have been studied (Fig. S1) [25–41]. In this ternary systems, organic chromophores process a strong absorption in the UV region and are excited to singlet state ($^1\pi\pi^*$); intersystem crossing to triplet state ($^3\pi\pi^*$) and subsequently fast transfer energy to sensitize emissions of Ln^{3+} ions by through-bond Dexter-type energy transfer [27,42]. In 2005, Francesconi et al. introduced sensitizing organic ligand into Ln-POM to construct organic-inorganic hybrid covalent bridging chromophore-Ln-POM ternary systems but not structurally characterized, where the Ln^{3+} ion was bound to POM building block as well as to the sensitizing organic ligand [27]. The high-efficiency organic chromophores ligands absorb UV light and is excited to singlet state, subsequently intersystem crossing to triplet state and energy transfer to Ln^{3+} ion. In 2010, Boskovic and coworkers reported two Tb-center chromophores-Tb-POM ternary systems, and the crystal structure of the system was firstly obtained [41]. The investigations reveal the sensitization of Tb^{3+} ions proceeds through the organic picolinate ligands and does not involve POM-centered LMCT states, and POM can quench the luminescence of Tb^{3+} ions due to non-radiation deactivation involving Tb^{IV}–W^{V} charge-transfer (CT) state. As an extension of this work, Boskovic and coworkers reported another three chromophore-Tb-POM compounds in 2012, and the photophysical investigation showed that both organic ligands and inorganic POM ligands sensitize the luminescence of Ln^{3+} ions [38]. In 2017, Zhou and coworkers obtained 3D metal-organic open frameworks based on Ln^{3+} ions and Anderson-type POM, and the energy transfer mechanism from organic nicotinate ligand and POM moiety to Tb^{3+} or Eu^{3+} ions have been investigated [40]. Furthermore, the color-tunable luminescence properties also can be well tuned by simply adjusting the molar ratio of La^{3+}, Tb^{3+} and Eu^{3+} ions within the molecule.

In this paper, we choose lacunary $K_{14}[P_2W_{19}O_{69}(H_2O)]{\cdot}24H_2O$ POM precursor that can provide abundant POM-fragmented building blocks in solution reacts with $LnCl_3{\cdot}6H_2O$ and benzoic acid to successfully synthetize a series of chromophore-Ln-POM $[N(CH_3)_4]_3K_2Ln(C_7H_5O_2)(H_2O)_2(\alpha\text{-}PW_{11}O_{39})]{\cdot}11H_2O$ (Ln^{3+} = Eu^{3+} (**1**), Tb^{3+} (**2**), Tm^{3+} (**3**), Lu^{3+} (**4**)). The resulting compounds were characterized by elemental analysis, single crystal X-ray diffraction, IR spectra, powder X-ray diffraction (PXRD), thermogravimetric analyses (TGA). The photoluminescence properties of **1**–**4** also have been studied. Subsequently, a series of multicenter-Ln analogues $[N(CH_3)_4]_3K_2Eu_xTb_yTm_{1-x-y}(C_7H_5O_2)(H_2O)_2(\alpha\text{-}PW_{11}O_{39}){\cdot}11H_2O$ (**5**–**11**) were synthesized by tuning the molar ratio of Eu^{3+}:Tb^{3+}:Tm^{3+} ions during the process of synthesis. A simple red from Eu^{3+} emitting center, green from Tb^{3+} emitting center and blue from Tm^{3+} emitting center (RGB) mixing approach in the design of multicenter white-luminescent materials with expected luminescence were successfully prepared with careful adjustment of the molar concentration of Eu^{3+}:Tb^{3+}:Tm^{3+} ions within the same molecule. Furthermore, the energy transfer mechanism from POM and/or organic ligands to Ln^{3+} ions and also between different types of Ln^{3+} ions in the multicenter-Ln compounds were systematically studied by excitation spectra, emission spectra, variations of luminescence lifetime and time-resolved emission spectroscopy (TRES).

2. Experimental details

2.1. Materials and physical methods

All chemicals were commercially purchased and used without any further purification. The precursor $K_{14}[P_2W_{19}O_{69}(H_2O)]{\cdot}24H_2O$ was prepared on account of the document and confirmed by IR spectrum [43]. C, H, and N elemental analyses were performed using an Elementar Vario EL cube CHNS analyzer. Analyses for Eu, Tb and Tm atoms were recorded using a PerkinElmer Optima 2000 ICP-OES spectrometer (Table S1). PXRD data were collected on an X-ray powder diffractometer (Bruker, D8 Advance) using Cu Kα radiation (λ = 1.5418 Å) collected with the angular range (2θ) from 5° to 45° at room temperature. IR spectra were performed using a Bruker VERTEX-70 spectrometer using KBr pellets in the region of 400–4000 cm^{-1}. TGA cures were recorded from room 25 °C to 800 °C with a heating rate of 10 °C min^{-1} in flowing N_2 atmosphere on a NETZSCH STA 449 F5 Jupiter thermal analyzer.

2.2. Syntheses of **1**

$EuCl_3{\cdot}6H_2O$ (0.228 g, 0.600 mmol) was dissolved in water (30 mL), followed by the solid addition of benzoic acid (0.240 g, 0.200 mmol) and $K_{14}[P_2W_{19}O_{69}(H_2O)]{\cdot}24H_2O$ (2.120 g, 0.465 mmol) were added. The mixed solution stirred constantly to obtain a clear solution. Finally, the pH value of the clear solution was adjusted to 3.2–3.5 by 3 mol·L^{-1} KOH solution. The resulting solution was heated to 60 °C for about 1.5 h, and then tetramethylammonium chloride (TMACl) (0.110 g, 1.000 mmol) was added and stirred for about 30 min (Fig. S2). The resulting solution was cooled and filtered to evaporate at room temperature. The clear filtrate was left for about two weeks to gain colorless block crystals. Yield: 26.8% (0.560 g, based on $EuCl_3{\cdot}6H_2O$). Selected IR (KBr, cm^{-1}): 3437 (br), 3046 (w), 1642 (s), 1590 (m), 1521 (s), 1488 (s), 1422 (s), 1095 (s), 1050 (s), 951 (s), 895 (s), 828 (s) and 717 (m). Elemental analyses (%): Calcd, C, 6.55; H, 1.94; N, 1.20; Found, C, 6.75; H, 1.82; N, 1.22.

2.3. Syntheses of **2**–**11**

The synthesis of **2** is similar to **1** except for $EuCl_3{\cdot}6H_2O$ replaced by $TbCl_3{\cdot}6H_2O$ in rational proportions. Yield: 24.2% (0.507 g, based on $TbCl_3{\cdot}6H_2O$). Selected IR (KBr, cm^{-1}): 3439 (br), 3045 (w), 1636 (s), 1593 (m), 1527 (s), 1482 (s), 1423 (s), 1096 (s), 1045 (s), 956 (s), 895 (s), 830 (s) and 712 (m). Elemental analyses (%): Calcd, C, 6.53; H, 1.93; N, 1.20; Found, C, 6.65; H, 1.77; N, 1.25. The synthesis of **3** is similar to **1** except for $EuCl_3{\cdot}6H_2O$ replaced by $TmCl_3{\cdot}6H_2O$ in rational proportions. Yield: 29.5% (0.550 g, based on $TmCl_3{\cdot}6H_2O$). Selected IR (KBr, cm^{-1}): 3439 (br), 3046 (w), 1632 (s), 1588 (m), 1527 (s), 1488 (s), 1418 (s), 1095 (s), 1044 (s), 956 (s), 889 (s), 828 (s) and 713 (m). Elemental analyses (%): Calcd, C, 6.52; H, 1.93; N, 1.20; Found, C, 6.70; H, 1.75; N, 1.26. The synthesis of **4** is similar to **1** except for $EuCl_3{\cdot}6H_2O$ replaced by the mixture of $LuCl_3{\cdot}6H_2O$ in rational proportions. Yield: 23.3% (0.490 g, based on LuCl3·$6H_2O$). Selected IR (KBr, cm^{-1}): 3456 (br), 3040 (w), 1632 (s), 1589 (m), 1521 (s), 1490 (s), 1422 (s), 1096 (s), 1050 (s), 950 (s), 888 (s), 828 (s) and 712 (m). Elemental analyses (%): Calcd, C, 6.51; H, 1.93; N, 1.20; Found, C, 6.80; H, 1.72; N, 1.22. The synthesis of **5**–**11** is similar to **1** except for $EuCl_3{\cdot}6H2O$ replaced by the mixture of $EuCl_3{\cdot}6H_2O$, $TbCl_3{\cdot}6H_2O$ and $TmCl_3{\cdot}6H_2O$ in rational proportions. **5:** Yield: 30.9% (0.587 g, based on $EuCl_3{\cdot}6H_2O$ (0.045 g, 0.120 mmol), $TbCl_3{\cdot}6H_2O$ (0.069 g, 0.180 mmol) and $TmCl_3{\cdot}6H_2O$ (0.114 g, 0.300 mmol)). Selected IR (KBr, cm^{-1}): 3445 (br), 3040 (w), 1637 (s), 1590 (m), 1520 (s), 1490 (s), 1425 (s), 1094 (s), 1050 (s), 952 (s), 899 (s), 825 (s) and 710 (m). Elemental analyses (%): Calcd, C, 6.53; H, 1.93; N, 1.20; Found, C, 6.78; H, 1.74; N, 1.26. **6:** Yield: 23.8% (0.484 g, based on $EuCl_3{\cdot}6H_2O$ (0.069 g, 0.180 mmol), $TbCl_3{\cdot}6H_2O$ (0.045 g, 0.120 mmol) and $TmCl_3{\cdot}6H_2O$ (0.114 g, 0.300 mmol)). Selected

IR (KBr, cm^{-1}): 3445 (br), 3040 (w), 1642 (s), 1592 (m), 1525 (s), 1489 (s), 1422 (s), 1096 (s), 1049 (s), 950 (s), 894 (s), 826 (s) and 715 (m). Elemental analyses (%): Calcd, C, 6.52; H, 1.93; N, 1.20; Found, C, 6.82; H, 1.69; N, 1.30. **7:** Yield: 26.9% (0.564 g, based on $EuCl_3{\cdot}6H_2O$ (0.023 g, 0.060 mmol), $TbCl_3{\cdot}6H_2O$ (0.045 g, 0.120 mmol) and $TmCl_3{\cdot}6H_2O$ (0.160 g, 0.420 mmol)). Selected IR (KBr, cm^{-1}): 3440 (br), 3046 (w), 1645 (s), 1590 (m), 1521 (s), 1487 (s), 1423 (s), 1090 (s), 1050 (s), 950 (s), 896 (s), 826 (s) and 714 (m). Elemental analyses (%): Calcd, C, 6.52; H, 1.93; N, 1.20; Found, C, 6.78; H, 1.68; N, 1.30. **8:** Yield: 21.4% (0.450 g, based on $EuCl_3{\cdot}6H_2O$ (0.007 g, 0.018 mmol), $TbCl_3{\cdot}6H_2O$ (0.039 g, 0.102 mmol) and $TmCl_3{\cdot}6H_2O$ (0.182 g, 0.480 mmol)). Selected IR (KBr, cm^{-1}): 3445 (br), 3045 (w), 1645 (s), 1590 (m), 1519 (s), 1489 (s), 1422 (s), 1098 (s), 1050 (s), 955 (s), 898 (s), 829 (s) and 717 (m). Elemental analyses (%): Calcd, C, 6.52; H, 1.93; N, 1.20; Found, C, 6.82; H, 1.72; N, 1.23. **9:** Yield: 22.8% (0.480 g, based on $EuCl_3{\cdot}6H_2O$ (0.005 g, 0.012 mmol), $TbCl_3{\cdot}6H_2O$ (0.022 g, 0.060 mmol) and $TmCl_3{\cdot}6H_2O$ (0.200 g, 0.528 mmol)). Selected IR (KBr, cm^{-1}): 3442 (br), 3046 (w), 1645 (s), 1595 (m), 1521 (s), 1490 (s), 1425 (s), 1096 (s), 1050 (s), 950 (s), 894 (s), 830 (s) and 714 (m). Elemental analyses (%): Calcd, C, 6.52; H, 1.93; N, 1.20; Found, C, 6.79; H, 1.65; N, 1.20. **10:** Yield: 24.9% (0.523 g, based on $EuCl_3{\cdot}6H_2O$ (0.003 g, 0.006 mmol), $TbCl_3{\cdot}6H_2O$ (0.015 g, 0.042 mmol) and $TmCl_3{\cdot}6H_2O$ (0.209 g, 0.552 mmol)). Selected IR (KBr, cm^{-1}): 3447 (br), 3045 (w), 1645 (s), 1592 (m), 1525 (s), 1490 (s), 1422 (s), 1094 (s), 1045 (s), 958 (s), 890 (s), 830 (s) and 717 (m). Elemental analyses (%): Calcd, C, 6.52; H, 1.93; N, 1.20; Found, C, 6.85; H, 1.64; N, 1.28. **11:** Yield: 24.2% (0.510 g, based on $EuCl_3{\cdot}6H_2O$ (0.001 g, 0.003 mmol), $TbCl_3{\cdot}6H_2O$ (0.010 g, 0.027 mmol) and $TmCl_3{\cdot}6H_2O$ (0.217 g, 0.570 mmol)). Selected IR (KBr, cm^{-1}): 3440 (br), 3048 (w), 1645 (s), 1595 (m), 1520 (s), 1490 (s), 1424 (s), 1090 (s), 1050 (s), 950 (s), 898 (s), 828 (s) and 720 (m). Elemental analyses (%): Calcd, C, 6.52; H, 1.93; N, 1.20; Found, C, 6.87; H, 1.65; N, 1.27.

2.4. X-ray crystallography

A suitable sample of **1**–**4** were collected for the crystallographic study at 296(2) K and intensity data were collected on a Bruker Apex II CCD diffractometer at room temperature with graphite-monochromated Mo Kα radiation (λ = 0.71073 Å). Intensity data were corrected for Lorentz and polarization effects as well as for multi-scan absorption. The structure was solved by direct methods and heavy atoms were located by full matrix least-squares refinements on F^2 and Fourier syntheses using the SHELXS-1997 program package, which was further refined by full-matrix least squares on F^2 using the SHELXL-2018/1 program package [44]. In the final refinement cycles, all the non hydrogen atoms were refined anisotropically. The partial lattice water molecules were located by using a Fourier map and the remaining lattice water molecules were determined by TGA results. The hydrogen atoms of the mal groups and water molecules were placed in calculated positions and then refined using a riding model. Crystallographic data for **1**–**4** with CCDC number of 1,882,084–1,882,087 can be obtained free from the Cambridge Crystallographic Data Center. Crystallographic data and structure refinements for **1**–**4** are listed in Table 1.

2.5. Photoluminescence

Photoluminescence emission spectra, photoluminescence excitation spectra, decay time curves and TRES were recorded using an EDINBURGH FLS 980 fluorescence spectrophotometer equipped with a monochromated 325 W Xe-arc excitation source and a visible detector (Hamamatsu R928P). The single exponential function of decay time curve: $I(t) = Ae^{(-t/\tau)}$; where I(t) is the emission intensity at time t, A is the pre-exponential factor of lifetime τ. The double exponential function of decay time curve: $I(t) = A_1e^{(-t/\tau 1)} + A_2e^{(-t/\tau 2)}$; where I (t) represents the emission intensity at time t, A_1 and A_2 are the pre-exponential factors of lifetime τ_1 and τ_2. The average lifetime τ^* of are calculated by $\tau^* = (A_1\tau_1^2 + A_2\tau_2^2)/(A_1\tau_1 + A_2\tau_2)$ [45]. The CIE 1931 chromaticity coordinates were calculated on the basis of the international CIE standards.

3. Results and discussion

3.1. Powder X-ray diffraction

A comparison between the simulated powder diffraction patterns from the single-crystal X-ray diffraction structural analyses of **1** and the experimental powder diffraction diagram of **1**–**11** evidences that multicenter-Ln resulting samples are isostructural with the single crystal and all the experimental samples are in good phase purity (Fig. 1). In addition, the existence of different pattern intensity among the

Table 1
Crystal data for the **1**.

	1	**2**	**3**	**4**
Empirical formula	$C_{19}H_{67}EuK_2N_3O_{54}PW_{11}$	$C_{19}H_{67}TbK_2N_3O_{54}PW_{11}$	$C_{19}H_{67}TmK_2N_3O_{54}PW_{11}$	$C_{19}H_{67}LuK_2N_3O_{54}PW_{11}$
Formula weight	3485.10	3492.06	3502.7	3508.1
Temperature/K	296.15	296.15	296.15	296.15
Crystal system	Triclinic	Triclinic	Triclinic	Triclinic
Space group	P-1	P-1	P-1	P-1
a [Å]	12.9454 (14)	12.921 (3)	12.8403 (14)	12.946 (10)
b [Å]	13.5128 (14)	13.504 (3)	13.4246 (15)	13.602 (10)
c [Å]	20.206 (2)	20.156 (4)	19.981 (2)	20.190 (15)
α [°]	82.9783 (18)	82.918 (4)	83.917 (2)	82.829 (14)
B [°]	78.1714 (18)	78.077 (4)	78.657 (2)	78.213 (14)
γ [°]	75.1355 (18)	75.141 (3)	75.480 (2)	75.131 (14)
V [$Å^3$]	3334.7 (6)	3316.9 (12)	3263.3 (6)	3354 (4)
Z	2	2	2	2
ρ_{calcd} [g cm^{-3}]	3.381	3.406	3.472	3.385
μ [mm^{-1}]	20.058	20.287	20.895	20.480
F (*000*)	3012.0	3016.0	3024.0	3028.0
Index ranges	−15 ≤ h ≤ 15 −12 ≤ k ≤ 16 −24 ≤ l ≤ 24	−12 ≤ h ≤ 15 −12 ≤ k ≤ 16 −23 ≤ l ≤ 24	−15 ≤ h ≤ 15 −15 ≤ k ≤ 16 −23 ≤ l ≤ 17	−14 ≤ h ≤ 15 −16 ≤ k ≤ 16 −24 ≤ l ≤ 24
Reflections collected	17,402	17,306	16,656	17,500
Independent reflections	11,752 [R_{int} = 0.0314]	11,697 [R_{int} = 0.0753]	11,435 [R_{int} = 0.0398]	11,876 [R_{int} = 0.0575]
data/restraints/parameters	11,752/57/424	11,697/57/424	11,435/57/424	11,876/57/424
Goodness-of-fit on F^2	1.024	1.019	1.015	1.024
R_1, wR_2 [$I > 2\sigma(I)$]	0.0422, 0.0955	0.0682, 0.1534	0.0638, 0.1747	0.0618, 0.1186
R_1, wR_2 [all data]	0.0606, 0.1051	0.1206, 0.1875	0.0796, 0.1883	0.1158, 0.1453

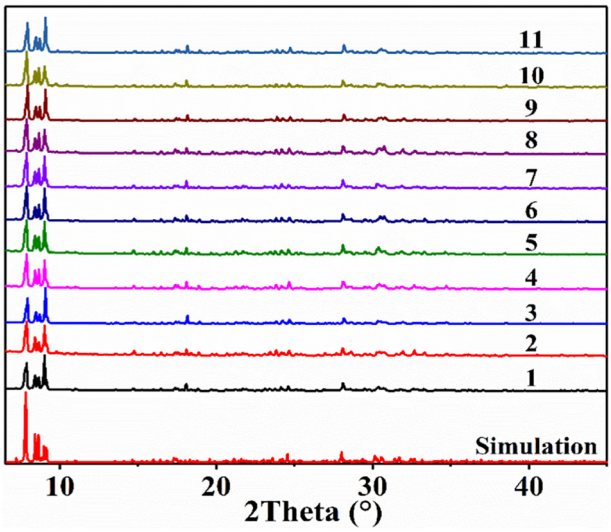

Fig. 1. Simulated single-crystal PXRD of **1** and experimental PXRD patterns of **1**–**11**.

simulated and experimental PXRD patterns may be on account of the variations in preferred orientation of the experimental samples during the process of collection of the PXRD patterns.

3.2. TGA measurement

The thermal stability of **1**–**4** was determined under the N_2 atmosphere between 25 and 1000 °C. As shown in Fig. S3, the curves of **1**–**4** display similar thermal stability and show three weight losses. The first stepweigh loss of 6.17% from 25 to 140 °C, corresponding to the removal of eleven lattice water (calcd 6.05%). The second step weigh loss of 7.83% from 140 to 490 °C towards two coordinated water ligands and oxidation of three $[N(CH_3)_4]^+$ (calcd 7.38%). The third step weigh loss from 490 to 890 °C can be attributed to the oxidation of organic benzoic acid and partial decomposition of POM skeleton.

3.3. Structure description

The PXRD patterns of **1**–**11** are well consistent with the simulated patterns that originated from the single-crystal X-ray diffraction data of **1**, indicating that **1**–**11** are isomorphic. Herein, only the structure of **1** was selected as representative for the detail description, which crystallize in P–1 space group of the triclinic system. **1** is comprised of one $[Eu(C_7H_5O_2)(H_2O)_2(\alpha\text{-}PW_{11}O_{39})]^{5-}$ polyanion, two K^+ ions, three $[N(CH_3)_4]^+$ and eleven lattice water molecules. As shown in Fig. 2 (a) and (b), one Eu^{3+} ion embeds into the vacant site of lacunary Keggin-type $(\alpha\text{-}PW_{11}O_{39})^{7-}$ subunit through four oxygen atoms, and one benzoic ligand coordinates to the Eu^{3+} ion through two carboxyl oxygen atoms to construct one ternary system of chromophore-Eu-POM. The angle of W—O—Eu bond range from 137.0(4)° to 157.4(5)°, and of C—O—Eu is in the range of 93.2(9)–93.4(8)°. The Eu center is surrounded by four oxygen atoms (O13, O16, O19, O30) from $(\alpha\text{-}PW_{11}O_{39})^{7-}$ subunit, two oxygen atoms (O40, O41) from benzoic carboxylate and two coordinated water oxygen atoms (O1W, O2W), in a distorted square antiprismatic configuration (Fig. 3c). The distance of Eu—O bond is in the range of 2.327(9)–2.513(10) Å, and the angel of O—Eu—O bond is between 52.3(3)° and 151.8(3)°. The adjacent two $[Eu(C_7H_5O_2)(H_2O)_2(\alpha\text{-}PW_{11}O_{39})]^{5-}$ polyanion of **1** can be connected by two K1 ions to form $[KLu(C_7H_5O_2)(\alpha\text{-}PW_{11}O_{39})]_2^{8-}$ building block (Fig. S4). Each K1 ion is four-coordinated bonding to one lattice water oxygen atom (O4W), two oxygen atoms (O6, O30) from two $(\alpha\text{-}PW_{11}O_{39})^{7-}$ subunits and one oxygen atom (O41) from benzoic ligand with the distance of K1—O ranging from 2.663(14) Å to 2.801(9) Å and angel of O—K1—O bond varying from 83.7(4) to 170.1(3) (Fig. S5).

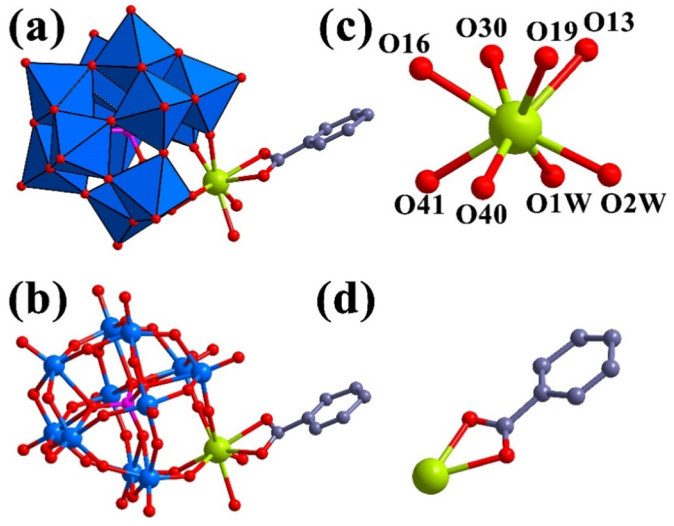

Fig. 2. (a) Polyhedral representation of the polyanion in **1**; (b) ball-and-stick representation of polyanion in **1**; (c) the coordination environment of Eu centre; (d) the coordination mode of benzoic ligands; (color codes: WO_6, blue; W, blue; P, pink; Eu, lime; O, red; C, blue gray).

3.4. IR spectra

1–**11** have similar IR spectra (Fig. S6) that match well with the results of PXRD and crystal structural analyses, therefore only IR spectrum of **1** was discussed in Fig. 3. IR spectra of **1**, $K_{14}[P_2W_{19}O_{69}(H_2O)]\cdot 24H_2O$ and benzoic ligand were measured in KBr pellets on a Bruker VERTEX 70 IR spectrometer from 450 to 4000 cm^{-1}. **1** has similar strong peaks with $K_{14}[P_2W_{19}O_{69}(H_2O)]\cdot 24H_2O$ precursor in the range of 700–1100 cm^{-1} that can be attributed to ν(P—O_a), ν(W—O_t), ν(W—O_b) and ν(W—O_c) vibrations bands of $(\alpha\text{-}PW_{11}O_{39})^{7-}$ groups [46]. The peaks ranging from 1400 cm^{-1} to 1600 cm^{-1} of **1** are attributed to the stretching band of aromatic ring and δ(C—H) bending vibrations. The analogical peaks can be found in organic benzoic ligand, indicating the organic ligand appears in **1**. It should be noticed that the obvious ν(C═O) stretching band at 1692 cm^{-1} in IR spectrum of organic benzoic ligand, yet the insignificant peak at 1642 cm^{-1} can be observed in IR spectrum of **1**. The reason can be explained as: (1) the COO^- group binds to Eu^{3+} metal ion for constructing Eu—O—C—O four-membered ring that causes the weaken stretching vibration of C═O band, hence the ν(C═O) stretching band shifts to lower wavenumber at

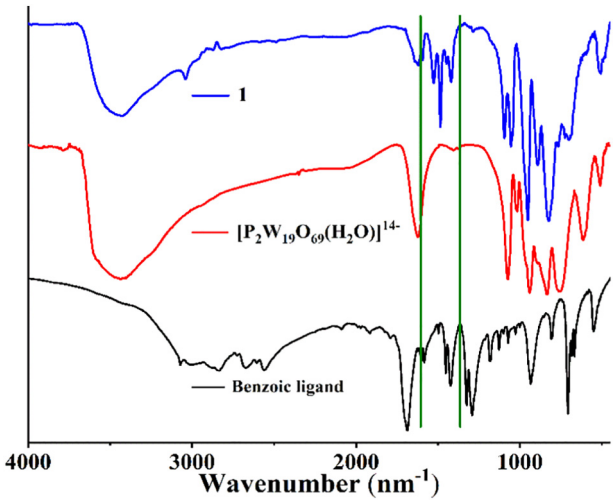

Fig. 3. IR spectra of **1**, $K_{14}[P_2W_{19}O_{69}(H_2O)]\cdot 24H_2O$ and benzoic ligand.

1642 cm^{-1}; (2) the δ(C—H) bending vibration peak apparently overlaps ν(C═O) stretching band in **1**. The above analyses manifest that the presences of POM fragments and organic ligand in **1**, are well consistent with the results of the structural analyses from single-crystal X-ray diffraction.

3.5. Photoluminescence properties

The photoluminescence behaviours of Ln-POM derivatives have been reported and systematically investigated in recent decades. Since the first Ln-substituted POMs $[LnW_{10}O_{36}]^{9-}$ (Ln = La^{3+}, Ce^{3+}, Pr^{3+}, Nd^{3+}, Sm^{3+}, Ho^{3+}, Er^{3+}, Yb^{3+}, and Y^{3+}) and $[LnW_{10}O_{36}]^{8-}$ (Ln = Ce^{4+}) were prepared by Peacock and Weakly in 1971 [47], the photoluminescence properties and energy transfer mechanism within Ln-POM have been attracting considerable interest [48,49]. Generally, the luminescence of Ln^{3+} can be sensitized by the O → M LMCT photoexcitation of POM component under UV irradiation. In the chromophores-Ln-POM "ternary systems", the luminescence of Ln^{3+} ion can be realized through sensitization via excitation of inorganic POM component and organic ligand. In the present works, **4** has been utilized to probe the excited energy level of POM and benzoic acid ligands to assess its efficiency in the energy transfer process to the Ln^{3+} ions. It could be noted that **4** is a suitable choice for elucidating excited level of POM and organic ligand for the reasons: the electron configuration of Lu^{3+} ion is full, and there is no emission of Lu^{3+} ion existed in the visible range, hence all luminescence observed could be attributed to POM component and/or organic ligand in the complexes. Moreover, the photoluminescence of Ln-based complexes are sensitive to the coordinated water molecules and angle of Ln—O—W bond within Ln-based molecule. When the aqua and similar molecules were coordinated to Ln^{3+} ion, the luminescence of Ln^{3+} emitting centre quenches as a consequence of the coupling with high O—H oscillators [50]. When the bond angles of Ln—O—W bond are approximately 150°, which can quench the luminescence of Ln^{3+} ion due to effective d^1 electrons hopping through electron delocalization and fπ–pπ–dπ orbital mixing [51,52]. In this series of **1**–**4**, the two water molecules bonded into Ln^{3+} ion may affect the luminescence of Ln^{3+} ion. Furthermore, the four angles of Ln—O—W bond are ~137.0 (4), ~137.2 (5), ~156.0 (5) and ~157.4 (5), respectively, which can to some extent affect but not facilitate the quenching of luminescence of Ln^{3+} ion.

The steady state excitation and emission spectra of **4** were recorded at room temperature. The emission spectra of **4** displays a broad band centered at 400 nm after excitation at 272 nm (Fig. S7), which can be assigned to the emission of organic benzoic ligands. To confirm the conjecture, the excitation and emission spectra of benzoic acid ligands also have been detected (Fig. S8). The shifts of peaks in emission spectra

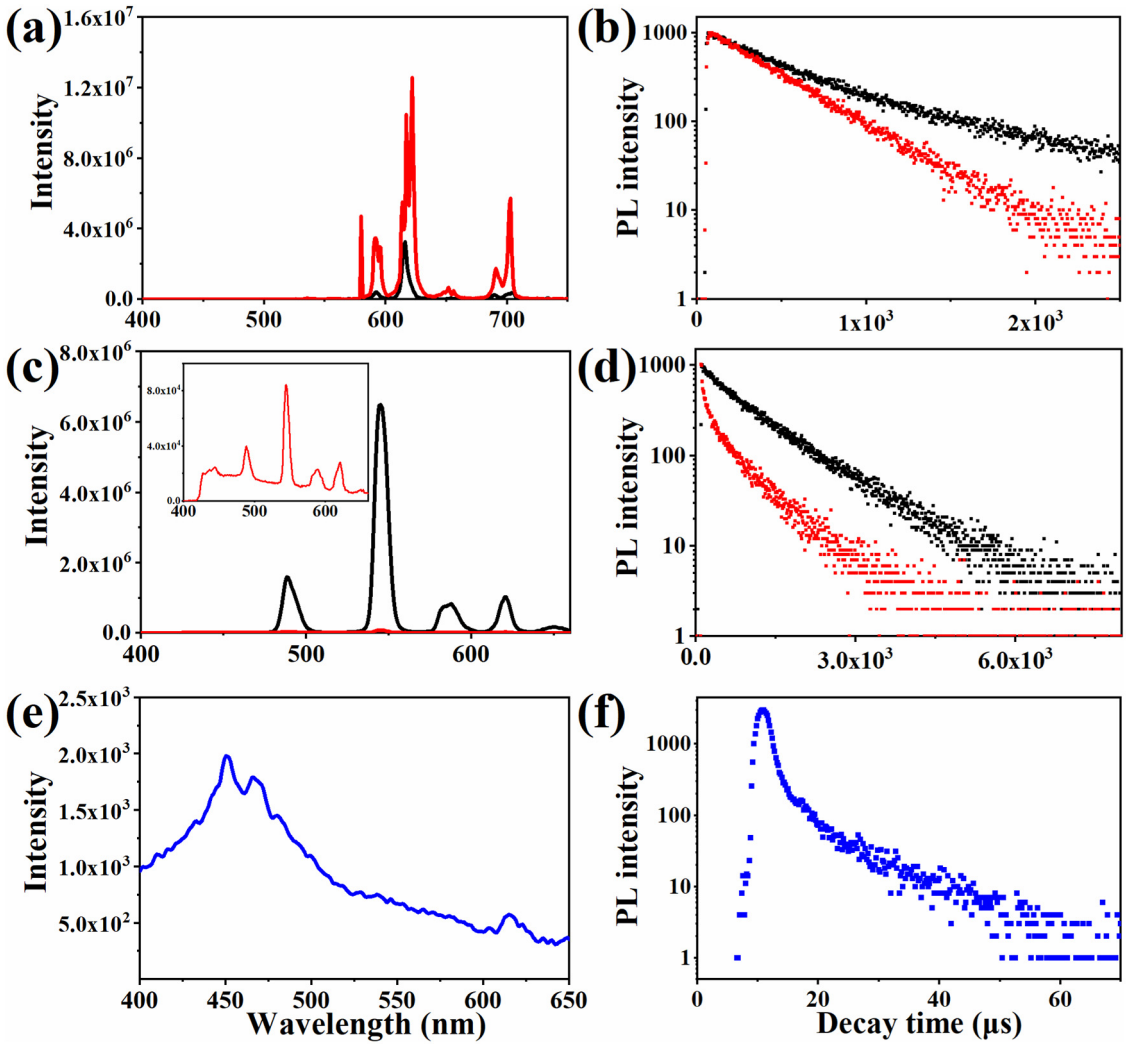

Fig. 4. (a) the emission spectra of **1** recorded under excitation at 272 nm (black line) and 395 nm (red line); (b) decay time curve of **1** monitored under excitation at 272 nm and emission at 616 nm (black line) and under excitation at 395 nm and emission at 620 nm (red line); (c) the emission spectra of **2** recorded under excitation at 272 nm (black line) and 378 nm (red line); (d) decay time curve of **2** monitored under excitation at 272 nm and emission at 546 nm (black line) and under excitation at 378 nm and emission at 546 nm (red line); (e) the emission spectra of **3** recorded under excitation at 272 nm (blue line); (f) decay time curve of **3** monitored under excitation at 272 nm and emission at 452 nm (blue line).

between **4** and organic benzoic ligand may be due to the coordination effect between metal ions and organic ligands. To elucidate energy transfer mechanism, it was best to determine the single and triplet energy level of the ligand. The singlet energy level of the ligand was determined by the excited absorption edge of **4**, and the value was found to be 307 nm (32,573 cm^{-1}) (Fig. S7a). The triplet energy level of the organic ligand was estimated by reference to its lower-wavelength emission edge (365 nm, 27,397 cm^{-1}) of luminescence spectrum of **4** (Fig. S7b). It is well known that the efficiency ligand-to-metal energy transfer required a good intersystem-crossing efficiency, which is maximized when the energy difference between singlet and triplet states is close to 5000 cm^{-1}. It amounts to 5176 cm^{-1} in **4**, and hence the ligand has a good intersystem-crossing efficiency. Furthermore, the triplet energy level of the ligands is found to be higher than that of the emitting level of $^5D_0$ of Eu^{3+}, $^5D_4$ of Tb^{3+} and $^1D_2$ of Tm^{3+}, proving that the ligands could serve as an antenna material for photosensitization of and Eu^{3+}, Tb^{3+} and Tm^{3+} emitting centres in **1**, **2** and **3**.

The steady state excitation spectrum of **1** at room temperature, monitored under emission at 620 nm consists of a weak broad band and several intense narrow bands (Fig. S9). The broad band at 272 nm is attributed to the $\pi \rightarrow \pi^*$ transition of benzoic ligands, and the narrow bands are assigned to $^7F_0 \rightarrow {}^5D_4$ transition (360 nm), $^7F_0 \rightarrow {}^5G_2$ transition (380 nm), $^7F_0 \rightarrow {}^5L_6$ transition (395 nm), $^7F_0 \rightarrow {}^5D_3$ transition (410 nm), $^7F_0 \rightarrow {}^5D_2$ transition (470 nm) and $^7F_0 \rightarrow {}^5D_1$ transition (525 nm) of the f-f transitions of Eu^{3+} ions. Obviously, the f-f transitions are stronger than the absorption of the organic ligand, proving that luminescence sensitization via excitation of organic ligand is much less efficient than the direct excitation of the Eu^{3+} ion f-f transitions absorption level. When the emission spectrum of **1** was performed under the maximum direct transition at 395 nm, the emission spectrum consists of the first excited state, $^5D_0$, and the ground septet, ^7F_J (J = 0–4), of Eu^{3+} ion. The $^5D_0 \rightarrow {}^7F_0$ transition is very sharp and is situated at 582 nm. The moderated $^5D_0 \rightarrow {}^7F_1$ transition splits into two Stark components at 589 and 592 nm, indicating the asymmetric coordination environment of Eu^{3+} local site in **1** [53]. The most intense transition $^5D_0 \rightarrow {}^7F_2$ is comprised of three strong bands at 616, 618 and 620 nm, mainly leading to red luminescence (Fig. S10). The peak at about 650 nm may be attributed to the characteristic $^5D_0 \rightarrow {}^7F_3$ transition. It is also noted that two splitting peaks of $^5D_0 \rightarrow {}^7F_4$ transition occurs at 697 and 701 nm. The split of peaks may be also due to the lower symmetry around Eu^{3+} emitting atoms, which is well consistent with the analysis of crystal structure. In addition, **1** was recorded under excitation of organic ligand at 272 nm, and the emission spectrum consist of only several peaks at 592 nm ($^5D_0 \rightarrow {}^7F_1$ transition), 616 nm ($^5D_0 \rightarrow {}^7F_2$ transition), 655 nm ($^5D_0 \rightarrow {}^7F_3$ transition) and splitting 697 and 701 nm ($^5D_0 \rightarrow {}^7F_4$ transition). The characteristic emission of $^5D_0 \rightarrow {}^7F_0$ transition could not be detected in the emission spectrum. In addition, the intensity of emission spectra under excitation at 272 nm is much lower than that under excitation at 395 nm (Fig. 4a). The transient-state photoluminescence emission spectra were also measured in Fig. 4b, which could be fitted by a single exponential function. The lifetime of **1** under excitation at 272 nm and emission at 620 nm is 1232.24 μs, while the lifetime under excitation at 395 nm and emission at 620 nm is 401.82 μs. The obvious difference of the lifetime effectively demonstrates different energy transfer pathway under different excitation, and also indicate organic benzoic ligands and POM components can active the luminescence of Eu^{3+} in **1**.

The steady state emission spectrum of **2** at room temperature is showed in Fig. 4c. The excitation spectrum of **2** was recorded upon the intense $^5D_4 \rightarrow {}^7F_5$ transition at 546 nm, which displays a prominent broad band at 272 nm and three very weak bands in the range of 330–400 nm (Fig. S11). The broad band at 272 nm could be ascribed to the $\pi \rightarrow \pi^*$ absorption of organic ligand, and the negligible bands between 330 and 400 nm were due to the $^7F_6 \rightarrow {}^5G_J$, $^7F_6 \rightarrow {}^5D_2$ and $^7F_6 \rightarrow {}^5D_3$ transition of the Tb^{3+} ion. The room-temperature emission spectrum of **2** upon excitation at 272 nm displays the characteristic emissions of Tb^{3+} ion at 490, 546, 595, 620 and 655 nm as a result of deactivation of the $^5D_4$ excited state to the ground state ^7F_J (J = 6, 5, 4, 3, 2) of Tb^{3+} ion, which leads to a green emitting luminescence (Fig. S10). Moreover, the emission POM and/or organic ligand cannot be detected, indicating the presence of an efficient ligand-to-Tb^{3+} energy transfer process under excitation at 272 nm in **2**. As a contrast, the emission of **2** under excitation at 378 nm exhibits five sharp peaks at 490, 546, 595, 620 and 655 nm due to f-f transitions of Tb^{3+} ion and a broad band at around 430 nm assigned to inorganic and/or organic ligands. In addition, the lifetime of **2** under excitation 272 nm and 378 nm are 1039.57 and 715.71 μs, respectively (Fig. 4d), indicating the organic ligand can much more efficiently sensitize the luminescence of Tb^{3+} ion, which is good agreement with the previous works [27,42].

The excitation and emission spectra of **3** were also detected at the room temperature (Fig. S12 and Fig. 4e). The emission spectrum obtained under excitation at 272 nm shows the characteristic $^1D_2 \rightarrow {}^3F_4$ and $^1G_4 \rightarrow {}^3H_6$ f-f transition of Tm^{3+} ion at 452 and 475 nm, which can result in a blue emitting luminescence (Fig. S10). A considerably broad band from 400 nm to 500 nm may be due to the overlapping emissions of POM components, organic benzoic ligand and Tm^{3+} emitting centres. The excitation spectrum of **3** was recorded under the emission at 452 nm, and the excitation spectrum contains a broad absorption peaks below 300 nm and the characteristic $^3H_6 \rightarrow {}^1D_2$ f-f transition at 352 nm, implying the organic ligands can transfer energy and sensitize the luminescence of Tm^{3+} ion. The decay time curves of **3** monitored at 452 nm under excitation 272 nm also have been explored (Fig. 4f), showing that the energy transfer from organic benzoic ligand to Tm^{3+} emitting ions in **3**.

3.6. Color-tuning properties

Color-tuning emissions of doubly doped or triply doped multiple Ln^{3+} ions in heteronuclear complexes have been widely investigated because they are proving broad using in the lighting materials [54–57]. Especially, the white light emission could come true based on mixed red-green-blue emitting color complexes, and only several white-light-emission complexes based on POM derivatives were reported now. In 2012, the first color-tunable emitting Ln-POMs, namely, $\{[Ln_2(DMF)_8(H_2O)_6][ZnW_{12}O_{40}]\}\cdot 4DMF$ (Ln^{3+} = La^{3+}, Eu^{3+}, and Tb^{3+}) were first reported by Wu and coworkers, which display interesting color-tunable and white-light-emitting behaviours [58]. Nevertheless, several DMF and H_2O molecules enter into the Ln^{3+} ion coordination surroundings, which can result in nonradiative deactivation of the excited level of Ln^{3+} ion via high O − H vibrations. Aforementioned, Zhou and coworkers reported a series of isostructural $Na(HL)(CH_3COO)Eu_mTb_nLa_{1-m-n}(AlMo_6(OH)_6O_{18})(H_2O)_6\cdot 10H_2O$ (L = nicotinate) in 2017, which display tunable luminescence color behaviour including white light emitting emissions [40]. In 2018, Zhou and coworkers reported another white-light emitting thin films based on pure inorganic POM $Na_9Eu_mTb_nCe_{1-m-n}W_{10}O_{36}$ [24], and no chromophore ligands coordinated to Ln^{3+} ions efficiently involve the sensitization of Tb^{3+}/Eu^{3+}/Ce^{3+} ions. Recently, our group reported a series of Tm^{3+}/Dy^{3+} codoped double-tartaric bridging POM derivative [50]. Investigations of photoluminescence emissions reveal that the Tm^{3+}/Dy^{3+}-POM can exhibit color-tunable photoluminescence behaviours, emitting color ranging from blue, through white, to yellow. The exploration of energy transfer indicates the O → M LMCT excited state of POM fragments can active Tm^{3+} and/or Dy^{3+} ions, and the energy can also transfer from Tm^{3+} to Dy^{3+} ions to efficiently accelerate emissions of the Dy^{3+} emitting centres.

Herein, the white-light-emitting properties of the Eu^{3+}/Tb^{3+}/Tm^{3+} codoped multicenter Ln-POM derivatives could be achieved through optimization of relative components of Eu^{3+}/Tb^{3+}/Tm^{3+} ions. As shown in Fig. 5a, it can be found that several sharp emission bands from Eu^{3+}/Tb^{3+}/Tm^{3+} ion and a relatively broad-band emission from organic benzoic ligand and inorganic POM group appear in the emission

spectra of the **5**–**11**. The white-light-emitting can be well tuned by adjusting the relative molar ratio of $Eu^{3+}/Tb^{3+}/Tm^{3+}$ components, which provides the basis to compensate the red emitting color from Eu^{3+} center, the green emitting color from Tb^{3+} center, and the blue emitting color of the overlap of Tm^{3+} center, organic and inorganic ligands under excitation at 272 nm ultraviolet light. When the Tm^{3+} ion's doping concentration is fixed at 0.5, the Tb^{3+} ion's doping component y increases, and the luminescence color of triply doped Eu/Tb/Tm-POM can be tuned from red (**1**; 0.663, 0.335), through orange-red (**5**; 0.489, 0.429), to green-yellow (**6**; 0.375, 0.506). Relatively, when the Tm^{3+} ion's doping concentration increases, the Eu^{3+} and Tb^{3+} ions' doping concentrations decrease, and the luminescence emitting color can be tuned from green-yellow (**6**; 0.375, 0.506), through white (**9**; 0.300, 0.337), to blue (**11**; 0.269, 0.290) within Eu/Tb/Tm-POM molecules. The corresponding CIE coordinates and the CIE luminescent color coordinates were shown in Table 2 and Fig. 5b, respectively. Based on the above results, it is known that **9** with the optimized molar ratio of $Eu^{3+}/Tb^{3+}/Tm^{3+}$ = 0.06:0.10:0.84 emits white color when the Eu/Tb/Tm-POM was excited at 272 nm. The calculated chromaticity coordinate of light emission of **9** fall within the white-light area of the CIE chromaticity diagram (0.300, 0.337), which is very closed to the standard white light (0.333, 0.333).

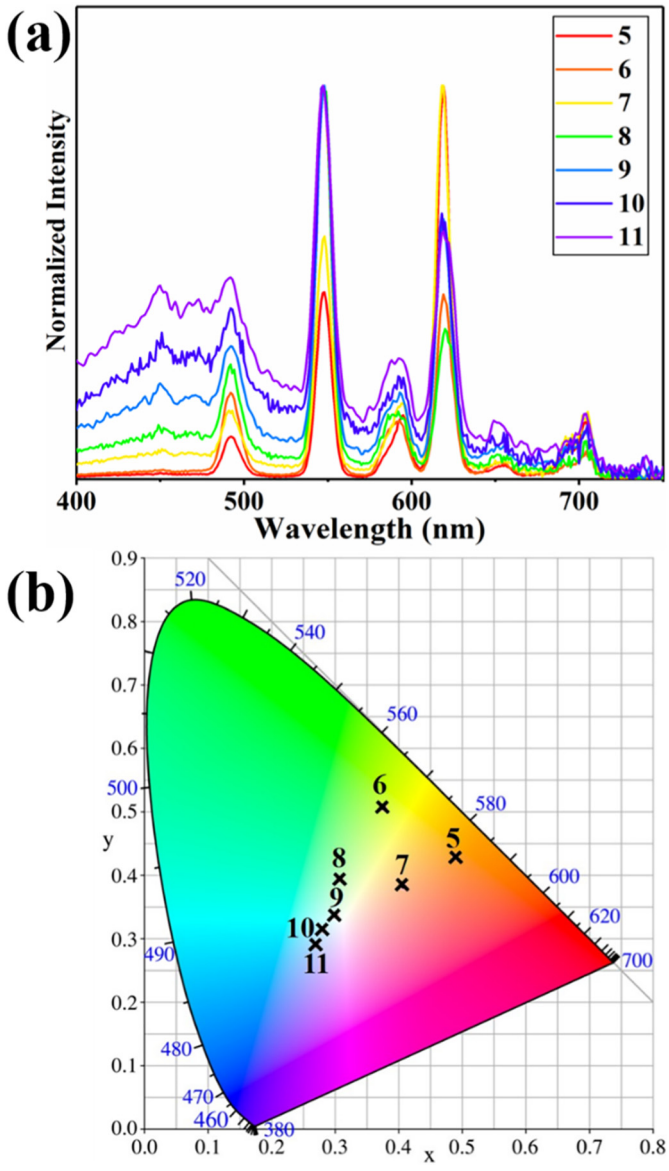

Fig. 5. (a) Photoluminescence emission spectra of **5**–**11** powder sample under excitation at 272 nm; (b) CIE chromaticity diagram corresponds to emissions of **5**–**11**.

Table 2
CIE chromaticity coordinates and emitting color of **1**–**3**, **5**–**8**.

Samples	(x, y)	Luminescence color
1	0.663, 0.335	Red
2	0.324, 0.591	Green
3	0.217, 0.210	Blue
5	0.489, 0.429	Orange-red
6	0.375, 0.506	Green-yellow
7	0.407, 0.382	Red
8	0.307, 0.394	Green-white
9	0.300, 0.337	White
10	0.279, 0.315	White-blue
11	0.269, 0.290	Blue

3.7. Energy transfer mechanism study

Energy transfer involving in multiple Ln^{3+} ions has been investigated, and the remarkable enhancements and quenching of the photoluminescence emissions also noticed in multicenter Ln-based complexes [59,60]. In the earlier studies, Yamase and coworkers have reasonably explored and summarized energy transfer mechanisms from O → M (M = Mo, W, V, Nb) LMCT triplet state through the singlet states along with a Förster-Dexter dipole-dipole type of coupling between the donor and the acceptor [42]. Building upon our previous work on energy transfer mechanism from POM fragments to Ln^{3+} ions, our group investigated the energy transfer process monitored by TRES, indicating the O → W LMCT photoexcitation of POM can sensitize the emission of Ln^{3+} ions [46,50,54]. As the previous reports, POM can absorb energy through O → M LMCT transition, hence the energy level of POM could be excited from ground state $^1A_{1g}$ to $^1T_{1u}$ triplet state and then return to $^3T_{1u}$ triplet state through fast nonradiative process under UV irradiation [23]. Subsequently, the photoexcitation O → M LMCT $^3T_{1u}$ state of POM transfer energy to Ln^{3+} ion via antenna effect. The organic ligand could be regarded as another sensitizer in chromophores-Ln-POM system, and the energy transfer process for the sensitization of Ln^{3+} ion could be explained by the following steps: (1) the organic chromophore absorbs UV light, which leads to the excited singlet level (S_1); (2) intersystem crosses (ISC) from S_1 to triplet state (T_1); (3) energy could transfer from the T_1 state to the excited 4f states of the Ln^{3+} ion. In the chromophores-Ln-POM complexes, the intramolecular energy migration efficiency from the organic chromophore ligand to the central emitting Ln^{3+} ion is one of the fatal factors that influence the luminescent behaviours of the Ln^{3+} analogue.

In this paper, the luminescence of Ln^{3+} emitting centres sensitized by organic benzoic ligand and energy transfer among the multiple Ln^{3+} ions were systematically investigated within mixed Ln^{3+}-based POM derivatives. As shown in Fig. 6, the excitation spectra display the similar outlines under Eu^{3+} emission at 620 nm, Tb^{3+} emission at 620 nm, and Tm^{3+} emission at 620 nm, indicating the similar energy transfer mechanism for sensitizing the luminescence of Eu^{3+}, Tb^{3+}, and Tm^{3+} ions in **5**–**11**. Interestingly, the excitation intensity of broad band at 272 nm under Eu^{3+} emission at 620 nm generally decreases with the decreasing of Eu^{3+} ion component, implying the better energy transfer efficiency from organic benzoic ligand to Eu^{3+} ion (Fig. 6a).

Similarly, the phenomenon also appears in the excitation spectra under Tb^{3+} emission at 546 nm, demonstrating the organic ligand also can effectively sensitize the luminescence of Tb^{3+} emitting centres (Fig. 6b). However, no obvious broad bands at 272 nm were discovered in the excitation spectra of **5**–**11** under Tm^{3+} emission at 452 nm, which may be attributed to the lower energy transfer efficiency from organic benzoic ligand to Tm^{3+} ion (Fig. 6c). In addition, a broad excitation band observed from 400 to 500 nm in **5**–**11**, which can be overlapped by the emission of **4**, proving energy transfer process from organic/

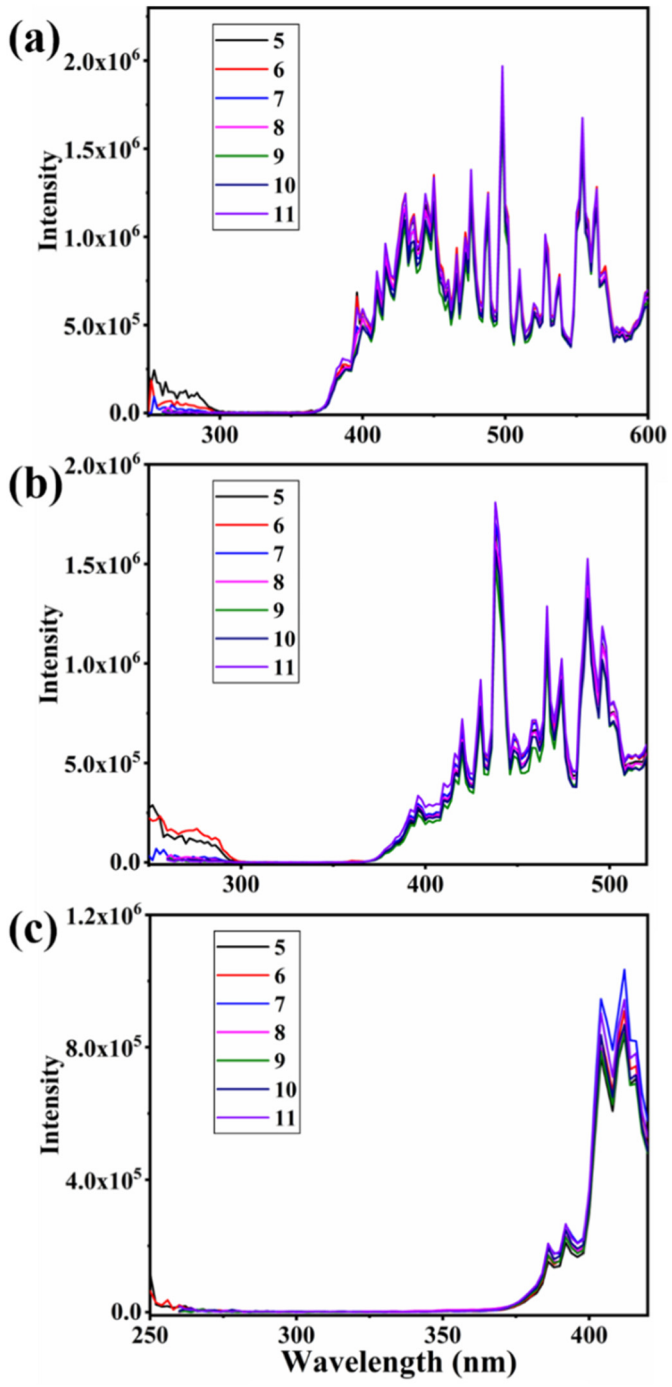

Fig. 6. The excitation spectra of **5**–**11** under emissions at 620 (a), 546 (b) and 452 nm (c).

inorganic ligands to Eu^{3+} and/or Tb^{3+} ion. All the above results show that the better sensitization efficiency from organic ligand to Eu^{3+} and/or Tb^{3+} ion rather than Tm^{3+} ion, which may be due to a lower excited energy from ground level to excited level of Eu^{3+} and/or Tb^{3+} ion.

Until now, the investigation of energy transfer mechanism among multiple Ln^{3+} ions in multicenter Ln-POM have been rarely reported. Recently, we reported the energy transfer from Tm^{3+} ion to Dy^{3+} ion in Tm/Dy-POM, which were demonstrated by TRES and decreased luminescence lifetime of Tm^{3+} ion with the addition of Dy^{3+} ion component. Here, the energy transfer mechanism among Eu^{3+}/Tb^{3+}/Tm^{3+} ions were systematically studied. As we know, the luminescence lifetime, as per the inherent nature of luminescent materials, can be regarded as an important technology for the exploration of energy

Table 3
The fitting results of **3**, **5**, **6**, **7**, **8**, **9**, **10**, **11** under excitation at 272 nm and emission at 452 nm.

Samples	τ_1 (μs)	α_1 (%)	τ_2 (μs)	α_2(%)	τ^* (μs)
3	0.92	65.73	7.84	34.27	6.56
5	0.97	64.88	6.51	35.12	5.32
6	1.02	67.27	6.69	32.73	5.33
7	0.91	66.16	7.10	33.84	5.86
8	0.76	69.48	6.69	30.52	5.47
9	1.02	68.01	6.25	31.99	4.90
10	1.35	69.97	6.36	30.03	4.70
11	1.28	65.76	6.58	34.24	5.13

transfer process in multiple-Ln^{3+} molecules. The luminescence lifetime of Tm^{3+} emitting centers in **5**–**11** have been detected, and the lifetime of Tm^{3+} emitting ions decreased with increasing of the total molar weight of Eu^{3+} and Tb^{3+} ions, indicating the energy can transfer from Tm^{3+} ions to Eu^{3+} and/or Tb^{3+} ions (Table 3). To demonstrate energy transfer relation between Tm^{3+}/Tb^{3+}, Tm^{3+}/Eu^{3+}, Eu^{3+}/Tb^{3+} ions, several doubly doped Eu/Tb-POM, Eu/Tm-POM, or Tb/Tm-POM have been further synthesized and explored in the context. First of all, the excitation and emission spectra of $Eu_{0.2}/Tb_{0.8}$-POM have been provided at room temperature (Fig. 7 and Fig. S13). For $Eu_{0.2}/Tb_{0.8}$-POM, the emission spectra present both the Tb^{3+} and Eu^{3+} characteristic f-f transition under excitation at 272 nm, exhibiting the energy can transfer from organic ligand to Tb^{3+} and Eu^{3+} ions (Fig. S13). The excitation spectra of $Eu_{0.2}/Tb_{0.8}$-POM also have been investigated under the Eu^{3+} emission at 620 nm (Fig. 7) and Tb^{3+} emission at 546 nm (Fig. S14). Meanwhile, the excitation spectrum under Tb^{3+} emission at 546 nm displays characteristic f-f excitation bands of Tb^{3+} ion, which is consistent with the excitation spectrum of **2** (Fig. S14), proving the same energy transfer pathway to sensitize the luminescence of Tb^{3+} ion in $Eu_{0.2}/Tb_{0.8}$-POM and **2** and no energy transfer involve from Eu^{3+} to Tb^{3+} ion. The excitation spectrum under Eu^{3+} emission at 620 nm shows both characteristic f-f excitation bands of Tb^{3+} and Eu^{3+} ion, implying the existence of energy could transfer from Tb^{3+} ion to Eu^{3+} ion but not from Eu^{3+} ion to Tb^{3+} ion within $Eu_{0.2}/Tb_{0.8}$-POM molecule (Fig. 7). That is to say, it is proposed that Tb^{3+} ion can assist sensitization of Eu^{3+} ion, which is in good agreement with the previous documents [61,62].[61,62] Similarly, the excitation and emission spectra of $Tb_{0.2}/Tm_{0.8}$-POM and $Eu_{0.1}/Tm_{0.9}$-POM also have been studied, and the results showed that the energy can transfer from organic components to Eu^{3+}/Tm^{3+} or Tb^{3+}/Tm^{3+} ion (Fig. S15–S18). The investigations of photoluminescence excitation and emission spectra of $Tb_{0.2}/Tm_{0.8}$-POM and $Eu_{0.1}/Tm_{0.9}$-POM

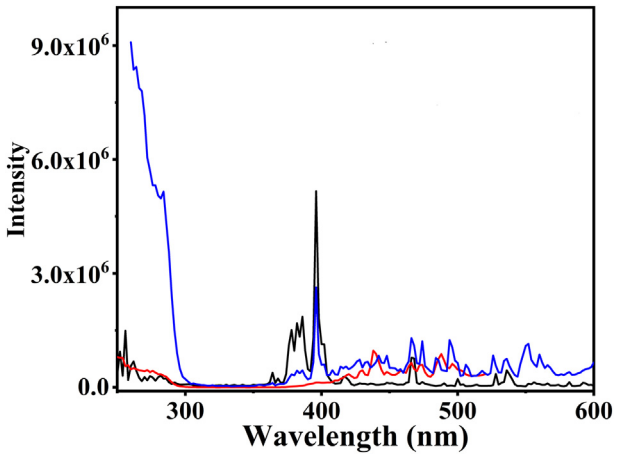

Fig. 7. The comparison of excitation spectra of **1** (black line) under emission at 620 nm and **2** (red line) under emission at 546 nm and $Eu_{0.2}/Tb_{0.8}$-POM (blue line) under emission at 620 nm.

indicate the Tm^{3+} ion cannot high-effectively sensitize the luminescence of Tb^{3+} and Eu^{3+} ion.

To further demonstrate energy transfer process, the TRES were also used to prove the energy transfer mechanism. As shown in Fig. 8a and Fig. 8b, the TRES of **9** was measured under excitation at 272 nm at room temperature. First of all, the obvious broad emissions band from 400 nm to 500 nm appear at 103.7 μs, and it is noted that the broad band assigned to the $\pi \rightarrow \pi^*$ transition emission of organic ligand and $^3T_{1u} \rightarrow {}^1A_{1g}$ transition resulting from the O → M LMCT triplet state of POM component is predominant in the spectrum (Fig. 8b). An unconspicuous peak appeared at 452 nm in the spectrum of 103.7 μs can be assigned to the characteristic f-f transfer of Tm^{3+} ion. As the time elapsed, the intensity of emission from 400 nm to 500 nm gradually increased, and the emission at 490 and 546 nm of Tb^{3+} ion f-f transitions, 592 and 620 nm of Eu^{3+} ion f-f transitions appeared at 111.7 μs. At 119.6 μs, the peak at 546 nm becomes more prominent, whereas the relative emission intensity from 400 nm to 500 nm observed with decline intensity. At 143.4 μs, the peak at 620 nm becomes prominent, and the emission from 400 nm to 500 nm generally disappears. Subsequently, the normalized intensity at 490 and 546 nm dropped down. All the above results indicate the energy transfer process from organic ligand and POM fragment, through Tm^{3+} and Tb^{3+} ion, to Eu^{3+} ion. Similar processes of spectral temporal evolution were detected for other Eu/Tb/Tm-POM (Fig. S19–25), which exhibit the observed time-resolved emission peaks with complex kinetics. The possible process of energy transfer shown in Fig. 9 to explain energy transfer pathway in **5**–**11** under irradiation. The TRES of $Eu_{0.2}/Tb_{0.8}$-POM, $Tb_{0.2}/Tm_{0.8}$-POM and $Eu_{0.1}/Tm_{0.9}$-POM also have been recorded to study the energy transfer mechanism between Eu^{3+}/Tb^{3+}, Tb^{3+}/Tm^{3+} and Eu^{3+}/Tm^{3+} ions (Fig. S26–S28). The results show the existence of energy transfer between different types of Ln^{3+} ions, and the schematic energy level diagram also have been summarized in Fig. S29–S31.

4. Conclusion

In summary, a series of $[N(CH_3)_4]_3K_2Ln(C_7H_5O_2)(H_2O)_2(\alpha\text{-}PW_{11}O_{39})]\cdot 11H_2O$ (Ln^{3+} = Eu^{3+} (**1**), Tb^{3+} (**2**), Tm^{3+} (**3**), Lu^{3+} (**4**)) samples were successfully prepared, which have been characterized by single crystal X-ray diffraction, elemental analysis, PXRD, TGA, and IR spectra. The photoluminescence excitation and emission spectra of

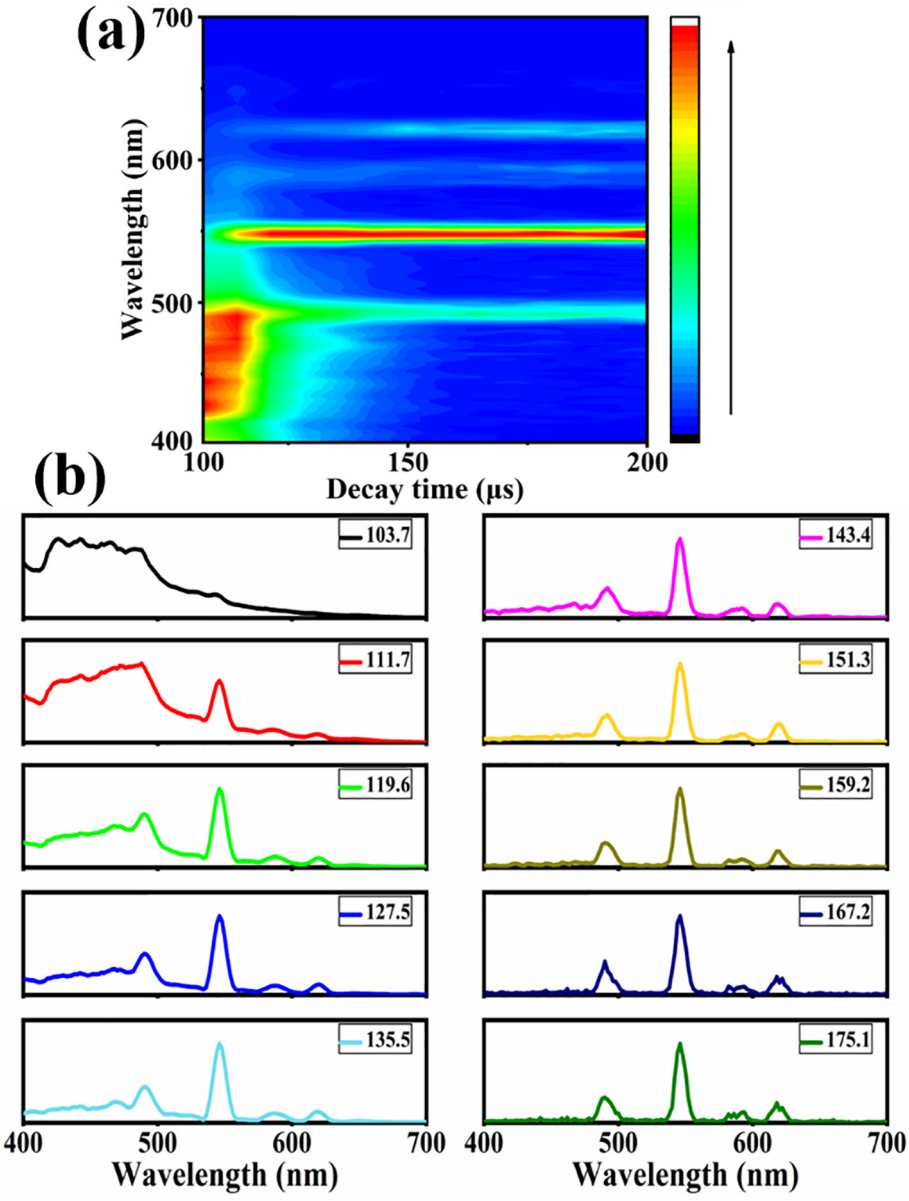

Fig. 8. (a) The TRES of **9** (λ_{ex} = 272 nm); (b) the emission spectrum of **9** at different time.

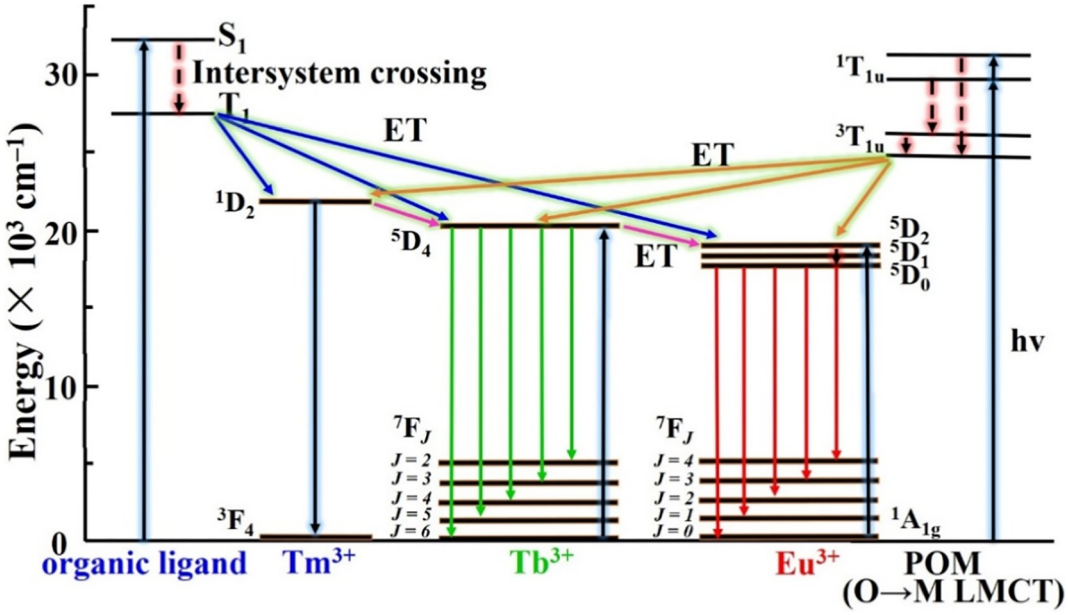

Fig. 9. Schematic energy level diagram and energy transfer process in **9**.

1–**4** were systematically investigated, proving the effective sensitization of organic ligand and POM fragment for Eu^{3+}, Tb^{3+} and Tm^{3+} ions. The investigations of Ln—O—W bond angles and coordinated water molecules indicate that the fπ-pπ-dπ orbital mixing and O—H oscillators may lead to luminescence quenching in this series of compounds. In addition, the multicenter-Ln analogues $[N(CH_3)_4]_3K_2Eu_xTb_yTm_{1-x-y}(C_7H_5O_2)(H_2O)_2(\alpha\text{-}PW_{11}O_{39})\cdot 11H_2O$ (**5**–**11**) also have been synthesized to study the white-light-emitting behaviours within Eu/Tb/Tm-POM molecules. The white-light-emitting behavior can be achieved by adjusting the molar ratio of $Eu^{3+}/Tb^{3+}/Tm^{3+} = 0.06:0.10:0.84$ in **9**. The energy transfer process from organic benzoic and POM ligand to Eu^{3+}, Tb^{3+}, and Tm^{3+} emitting centers were detected through the comparison of excitation of single-, double-, treble-Ln^{3+} mixed samples, indicating the energy could transfer from the photoexcitation O → M LMCT level of POM components and $\pi \rightarrow \pi^*$ transition of organic ligand to sensitize the luminescence emission of Ln^{3+} ions via intramolecular energy transitions. The energy transfer process between Eu^{3+}/Tb^{3+}, Tb^{3+}/Tm^{3+} and Eu^{3+}/Tm^{3+} ions also have been recorded and carefully studied by TRES and variation of Tm^{3+} luminescence lifetime, and the results show a low-effectively process of energy transfer between Tb^{3+}/Tm^{3+} and Eu^{3+}/Tm^{3+} ions and a relatively good energy transfer efficiency between Eu^{3+}/Tb^{3+} ions. Finally, the work provides a new synthetic strategy to research white-light-emitting properties in multicenter-Ln POM derivatives. Especially, the investigations of energy transfer mechanism among three types of Ln^{3+} ion in multicenter-Ln POMs have enriched the kinetic study of photoluminescence in luminescent POM materials.

Declaration of Competing Interest

The authors declare that they have no conflict of interest.

Acknowledgments

This work was financially supported by the National Natural Science Foundation of China (21771053, 21771054, 21571050 and 21573056), Natural Science Foundation of Henan Province (132300410144 and 162300410015), Henan Province Science and Technology Attack Plan Project (182102210237) and the 2018 Students Innovative Pilot Plan of Henan University (201810475016).

Appendix A. Supplementary data

Supplementary data to this article can be found online at https://doi.org/10.1016/j.saa.2019.117294.

References

[1] S. Pimputkar, J.S. Speck, S.P. DenBaars, S. Nakamura, Prospects for LED lighting, Nature photon 3 (2009) 180–182.
[2] P. Pust, V. Weiler, C. Hecht, A. Tücks, A.S. Wochnik, A.K. Henß, D. Wiechert, C. Scheu, P.J. Schmidt, W. Schnick, Narrow-band red-emitting $Sr[LiAl_3N_4]:Eu^{2+}$ as a next-generation LED-phosphor material, Nature Mate 13 (2014) 891–896.
[3] C.W. Yeh, W.T. Chen, R.S. Liu, S.F. Hu, H.S. Sheu, J.M. Chen, H.T. Hintzen, Origin of thermal degradation of $Sr_{(2-x)}Si_5N_8:Eu_{(x)}$ phosphors in air for light-emitting diodes, J. Am. Chem. Soc. 134 (2012) 14108–14117.
[4] X. Zhang, W. Liu, G.Z. Wei, D. Banerjee, Z. Hu, J. Li, Systematic approach in designing rare-earth-free hybrid semiconductor phosphors for general lighting applications, J. Am. Chem. Soc. 136 (2014) 14230–14236.
[5] S. Sivakumar, F.C.J.M. van Veggel, M. Raudsepp, Bright white light through up-conversion of a single NIR source from sol-gel-derived thin film made with Ln^{3+}-doped LaF_3 nanoparticles, J. Am. Chem. Soc. 127 (2005) 12464–12465.
[6] Q. Dai, M.E. Foley, C.J. Breshike, A. Lita, G.F. Strouse, Ligand-passivated $Eu:Y_2O_3$ nanocrystals as a phosphor for white light emitting diodes, J. Am. Chem. Soc. 133 (2011) 15475–15486.
[7] A.-Y. Ni, Y. Mu, J. Pan, S.-D. Han, M.-M. Shang, G.-M. Wang, An organic-inorganic hybrid zinc phosphite framework with room temperature phosphorescence, Chem. Commun. 54 (2018) 3712–3714.
[8] Y. Lv, L. Wang, Y. Zhuang, T.L. Zhou, R.J. Xie, Discovery of the Yb^{2+}–Yb^{3+} couple as red-to-NIR persistent luminescence emitters in Yb-activated $(Ba_{1-x}Sr_x)AlSi_5O_2N_7$ phosphors, J. Mater. Chem. C 5 (2017) 7095–7101.
[9] S. Li, Q. Zhu, D. Tang, X. Liu, G. Ouyang, L. Cao, N. Hirosaki, T. Nishimura, Z. Huang, R.-J. Xie, Al_2O_3–YAG:Ce composite phosphor ceramic: a thermally robust and efficient color converter for solid state laser lighting, J. Mater. Chem. C 4 (2016) 8648–8654.
[10] B.R. Judd, Optical absorption intensities of rare-earth ions, Phys. Rev. 127 (1962) 750–761.
[11] G.S. Ofelt, Intensities of crystal spectra of rare-earth ions, J. Chem. Phys. 37 (1962) 511–519.
[12] C.H. Huang, Rare Earth Coordination Chemistry: Fundamentals and Applications, John Wiley & Sons, Hoboken, NJ, 2010.
[13] W. Wei, G. Chen, A. Baev, G.S. He, W. Shao, J. Damascoand, P.N. Prasad, Alleviating luminescence concentration quenching in upconversion nanoparticles through organic dye sensitization, J. Am. Chem. Soc. 138 (2016) 15130–15133.
[14] P. Ma, F. Hu, J. Wang, J. Niu, Carboxylate covalently modified polyoxometalates: from synthesis, structural diversity to applications, Coord. Chem. Rev. 378 (2019) 281–309.
[15] Y. Liang, S. Li, D. Yang, P. Ma, J. Niu, J. Wang, Magnetic double-tartaric bridging mono-lanthanide substituted phosphotungstates with photochromic and switchable luminescence properties, J. Mater. Chem. C 4 (2016) 5424–5433.
[16] J. Lu, X. Ma, V. Singh, Y. Zhang, P. Ma, C. Zhang, J. Niu, J. Wang, Facile CO_2 cycloaddition to epoxides by using a tetracarbonyl metal selenotungstate derivate $[\{Mn(CO)_3\}_4(Se_2W_{11}O_{43})]^{8-}$, Inorg. Chem. 57 (2018) 14632–14643.

[17] Q. Han, W. Li, S.G. Wang, J. He, W. Du, M. Li, Asymmetric cascade catalysis with chiral polyoxometalate-based frameworks: sequential direct aldol and epoxidation reactions, ChemCatChem 9 (2017) 1801–1807.

[18] Q. Xu, Y. Niu, G. Wang, Y. Li, Y. Zhao, V. Singh, J. Niu, J. Wang, Polyoxoniobates as a superior Lewis base efficiently catalyzed knoevenagel condensation, Mol. Catal. 453 (2018) 93–99.

[19] X. Ma, W. Yang, L. Chen, J. Zhao, ChemInform abstract: significant developments in rare-earth-containing polyoxometalate chemistry: synthetic strategies, structural diversities and correlative properties, CrystEngComm 17 (2015) 8175–8197.

[20] P. Ma, F. Hu, Y. Huo, D. Zhang, C. Zhang, J. Niu, J. Wang, Magnetoluminescent bifunctional dysprosium-based phosphotungstates with synthesis and correlations between structures and properties, Cryst. Growth Des. 17 (2017) 1947–1956.

[21] T. Yamase, T. Kobayashi, M. Sugeta, H. Naruke, Europium(III) luminescence and intramolecular energy transfer studies of polyoxometalloeuropates, J. Phys. Chem. A 101 (1997) 5046–5053.

[22] Y. Liu, H. Li, C. Lu, P. Gong, X. Ma, L. Chen, J. Zhao, Organocounterions-assisted and pH-controlled self-assembly of five nanoscale high-nuclear lanthanide substituted heteropolytungstates, Cryst. Growth Des. 17 (2017) 3917–3928.

[23] T. Yamase, Photo- and electrochromism of polyoxometalates and related materials, Chem. Rev. 98 (1998) 307–325.

[24] H. Zhang, X. Li, L. Zhang, Y. Zhou, X. Ren, M. Liu, Color-tunable and white-light emitting thin films based on pure inorganic polyoxometalates $Na_9Eu_mTb_nCe_{1-m-n}W_{10}O_{36}$, J. Alloys Compd. 749 (2018) 229–235.

[25] S. Zhang, J. Zhao, P. Ma, J. Niu, J. Wang, Rare-earth-transition-metal organic-inorganic hybrids based on Keggin-type polyoxometalates and pyrazine-2,3-dicarboxylate, Chem. Asian J. 7 (2012) 966–974.

[26] H.L. Li, Y.J. Liu, J.L. Liu, L.J. Chen, J.W. Zhao, G.Y. Yang, Structural transformation from dimerization to tetramerization of serine-decorated rare-earth-incorporated arsenotungstates induced by the usage of rare-earth salts, Chem. Eur. J. 23 (2017) 2673–2689.

[27] C. Zhang, R.C. Howell, D. McGregor, L. Bensaid, S. Rahyab, M. Nayshtut, S. Lekperic, L.C. Francesconi, Synthesis of a cluster containing Eu(III) α_2-$P_2W_{17}O_{61}^{10-}$ and preliminary luminescence experiments, Comptes Rendus Chimie 8 (2005) 1035–1044.

[28] H. An, Y. Li, D. Xiao, E. Wang, C. Sun, Self-assembly of extended high-dimensional architectures from Anderson-type polyoxometalate clusters, Cryst. Growth Des. 6 (2006) 1107–1112.

[29] K. Wang, D. Zhang, J. Ma, P. Ma, J. Niu, J. Wang, Three-dimensional lanthanide polyoxometalate organic complexes: correlation of structure with properties, CrystEngComm 14 (2012) 3205–3212.

[30] S. Zhang, K. Wang, D. Zhang, P. Ma, J. Niu, J. Wang, 2-D and 3-D organic-inorganic hybrid lanthanide molybdates linking by pyridine-2,5-dicarboxylate, CrystEngComm 14 (2012) 8677–8683.

[31] S. Li, Y. Wang, P. Ma, J. Wang, J. Niu, From a versatile arsenotungstate precursor to a large lanthanide-containing polyoxometalate-carboxylate hybrid, CrystEngComm 16 (2014) 10746–10749.

[32] H. An, H. Zhang, Z. Chen, Y. Li, X. Liu, H. Chen, A series of three-dimensional architectures constructed from lanthanide-substituted polyoxometalosilicates and lanthanide cations or lanthanide-organic complexes as linkers, Dalton Trans. 41 (2012) 8390–8400.

[33] T. Yu, H. Ma, C. Zhang, H. Pang, S. Li, H. Liu, A 3d–4f heterometallic 3D POMOF based on lacunary Dawson polyoxometalates, Dalton Trans. 42 (2013) 16328–16333.

[34] M. Mirzaei, H. Eshtiagh-Hosseini, N. Lotfian, A. Salimi, A. Bauzá, R. Van Deun, R. Decadt, M. Barceló-Oliver, A. Frontera, Syntheses, structures, properties and DFT study of hybrid inorganic-organic architectures constructed from trinuclear lanthanide frameworks and Keggin-type polyoxometalates, Dalton Trans. 43 (2014) 1906–1916.

[35] Y. Lu, Y. Li, E. Wang, X. Xu, Y. Ma, A new family of polyoxometalate compounds built up of preyssler anions and trivalent lanthanide cations, Inorg. Chim. Acta 360 (2007) 2063–2070.

[36] H. Pang, Y. Chen, F. Meng, D. Shi, Assembly of three novel 2D frameworks with helical chains based on $[H_2W_{12}O_{40}]^{6-}$ clusters and lanthanide-organic complexes, Inorg. Chim. Acta 361 (2008) 2508–2514.

[37] D. Liu, Y. Lu, H. Tan, T. Wang, E. Wang, Series of organic-inorganic hybrid rare earth derivatives based on $[MnV_{13}O_{38}]^{7-}$ polyoxoanion: syntheses, structures, and magnetic and electrochemical properties, Cryst. Growth Des. 15 (2015) 103–114.

[38] C. Ritchie, V. Baslon, E.G. Moore, C. Reber, C. Boskovic, Sensitization of lanthanoid luminescence by organic and inorganic ligands in lanthanoid-organic-polyoxometalates, Inorg. Chem. 51 (2012) 1142–1151.

[39] X. Feng, W. Zhou, Y. Li, H. Ke, J. Tang, R. Clerac, Y. Wang, Z. Su, E. Wang, Polyoxometalate-supported 3d−4f heterometallic single-molecule magnets, Inorg. Chem. 51 (2012) 2722–2724.

[40] H. Ji, X. Li, D. Xu, Y. Zhou, L. Zhang, Z. Zuhra, S. Yang, Synthesis, structure, and photoluminescence of color-tunable and white-light-emitting lanthanide metal-organic open frameworks composed of $AlMo_6(OH)_6O_{18}^{3-}$ polyanion and nicotinate, Inorg. Chem. 56 (2017) 156–166.

[41] C. Ritchie, E.G. Moore, M. Speldrich, P. Kögerler, C. Boskovic, Terbium polyoxometalate organic complexes: correlation of structure with luminescence properties, Angew. Chem. Int. Ed. 49 (2010) 7702–7705.

[42] T. Yamase, Chapter 243 luminescence of polyoxometallolanthanoates and photochemical nano-ring formation. In Handbook on the Physics and Chemistry of Rare Earths; Elsevier, Vol. 39 (2009) pp 297–356.

[43] C.M. Tourne, G.F. Tourne, Aquanonadecatungstodiphosphate(14–) polyanion $[P_2W_{19}O_{69}(OH_2)]^{14-}$: X-ray crystallographic structure of its potassium salt, chemical relationships in the tungstophosphate system, and conversion into the diaquaicosatungstodiphosphate $[P_2W_{20}O_{70}(OH_2)_2]^{10-}$, J. Chem. Soc. Dalton Trans. (1988) 2411–2420.

[44] G.M. Sheldrick, SHELXT-integrated space-group and crystal-structure determination, Acta Crystallogr., Sect. C: Struct. Chem. C 71 (2015) 3–8.

[45] J. Zhang, G.M. Cai, L.W. Yang, Z.Y. Ma, Z.P. Jin, Layered crystal structure, color-tunable photoluminescence, and excellent thermal stability of $MgIn_2P_4O_{14}$ phosphate-based phosphors, Inorg. Chem. 56 (2017) 12902–12913.

[46] H. Wu, B. Yan, H. Li, V. Singh, P. Ma, J. Niu, J. Wang, Enhanced photostability luminescent properties of Er^{3+}-doped near-white-emitting $Dy_xEr_{(1-x)}$-POM derivatives, Inorg. Chem. 57 (2018) 7665–7675.

[47] R.D. Peacock, T.J.R. Weakley, Heteropolytungstate complexes of the lanthanide elements. Part I. preparation and reactions, J. Chem. Soc. A (1971) 1836–1839.

[48] P. Ma, Y. Si, R. Wan, S. Zhang, J. Wang, J. Niu, Synthesis, crystal structure, and properties of a 1-D terbium-substituted monolacunary Keggin-type polyoxotungstate, Spectrochim. Acta A 138 (2015) 579–584.

[49] P. Ma, R. Wan, Y. Si, F. Hu, Y. Wang, J. Niu, J. Wang, Double-malate bridging trilanthanoid cluster encapsulated arsenotungstates: syntheses, structures, luminescence and magnetic properties, Dalton Trans. 44 (2015) 11514–11523.

[50] H. Wu, M. Zhi, V. Singh, H. Li, P. Ma, J. Niu, J. Wang, Elucidating white light emissions in Tm^{3+}/Dy^{3+} codoped polyoxometalates: a color tuning and energy transfer mechanism study, Dalton Trans. 47 (2018) 13949–13956.

[51] B. Artetxe, S. Reinoso, L. San Felices, L. Lezama, J.M. Gutierrez-Zorrilla, J.A. García, J.R. Galan-Mascaró s, A. Haider, U. Kortz, C. Vicent, Cation-directed dimeric versus tetrameric assembliesof lanthanide-stabilized dilacunary Keggin tungstogermanates, Chem. Eur. J. 20 (2014) 12144–12156.

[52] B. Artetxe, S. Reinoso, L. San Felices, J.M. Gutierrez-Zorrilla, J.A. García, F. Haso, T. Liu, C. Vicent, Crown-shaped tungstogermanates as solvent-controlled dual systems in the formation of vesicle-like assemblies, Chem. Eur. J. 21 (2015) 7736–7745.

[53] S. Biju, N. Gopakumar, J.-C.G. Bünzli, R. Scopelliti, H.K. Kim, M.L.P. Reddy, Brilliant photoluminescence and triboluminescence from ternary complexes of Dy(III) and Tb(III) with 3-phenyl-4-propanoyl-5-isoxazolonate and a bidentate phosphine oxide coligand, Inorg. Chem. 52 (2013) 8750–8758.

[54] H. Wu, R. Wan, Y. Si, P. Ma, J. Wang, J. Niu, A helical chain-like organic-inorganic hybrid arsenotungstate with color-tunable photoluminescence, Dalton Trans. 47 (2018) 1958–1965.

[55] Y. Xiao, Z. Hao, L. Zhang, X. Zhang, G.H. Pan, H. Wu, H. Wu, Y. Luo, J. Zhang, An efficient green phosphor of Ce^{3+} and Tb^{3+}- codoped $Ba_2Lu_5B_5O_{17}$ and a model for elucidating the high thermal stability of the green emission, J. Mater. Chem. C 6 (2018) 5984–5991.

[56] X. Liu, C. Chen, S. Li, Y. Dai, H. Guo, X. Tang, Yu. Xie, L. Yan, Host-sensitized and tunable luminescence of $GdNbO_4$:Ln^{3+} (Ln^{3+} = Eu^{3+}/Tb^{3+}/Tm^{3+}) nanocrystalline phosphors with abundant color, Inorg. Chem. 55 (2016) 10383–10396.

[57] K. Li, X. Liu, Y. Zhang, X. Li, H. Lian, J. Lin, Host-sensitized luminescence properties in $CaNb_2O_6$:Ln^{3+} (Ln^{3+} = Eu^{3+}/Tb^{3+}/Dy^{3+}/Sm^{3+}) phosphors with abundant colors, Inorg. Chem. 54 (2015) 323–333.

[58] W. Zhao, C. Zou, L. Shi, J. Yu, G. Qian, C. Wu, Synthesis of diamondoid lanthanide-polyoxometalate solids as tunable photoluminescent materials, Dalton Trans. 41 (2012) 10091–10096.

[59] A.M. Kaczmarek, K.V. Hecke, R.V. Deun, Enhanced luminescence in Ln^{3+}-doped Y_2WO_6 (Sm, Eu, Dy) 3D microstructures through Gd^{3+} codoping, Inorg. Chem. 53 (2014) 9498–9508.

[60] M. Shang, C. Li, J. Lin, How to produce white light in a single-phase host? Chem. Soc. Rev. 43 (2014) 1372–1386.

[61] D. Ananias, F.A.A. Paz, D.S. Yufit, L.D. Carlos, J. Rocha, ChemInform abstract: photoluminescent thermometer based on a phase-transition lanthanide silicate with unusual structural disorder, J. Am. Chem. Soc. 137 (2015) 3051–3058.

[62] P. Chen, Q. Li, S. Grindy, N. Holten-Andersen, White-light-emitting lanthanide metallogels with tunable luminescence and reversible stimuli-responsive properties, J. Am. Chem. Soc. 137 (2015) 11590–11593.